

Supplementary Information for: On the Quantification of Hydrogen in Lithium Metal Oxides

Thomas Köhler,^{*a} Patrick Reichart,^b Erica Brendler,^c Anastasia Vyalikh,^{a,d} Andre Klostermeier,^e
Zdravko Siketić,^f Erik Mehner,^a Günther Dollinger,^b Hartmut Stöcker,^a and Dirk C. Meyer^a

S1 Error estimation for TOF-ERDA experiments

The total error consists of the spectrum statistical error, the error in the SRIM-2013 stopping power data¹ used for spectrum conversion in the Potku software², and the background subtraction error. If the spectrum count rate is high enough, the main limiting factor of the stoichiometry determination of thick samples by TOF-ERDA is the relative error of the ion stopping power, which is in the order of 6%¹.

In addition, it should be noted that the background events (visible in Fig. 2 a) between TOF channels 500 and 1000 are mainly caused by random coincidences arising from the high count rate of scattered primary ions on tantalum or niobium. In particular, for hydrogen measurements, the error in the final hydrogen concentration is much higher than the ~ 6% accuracy, because the noise below the hydrogen events (random coincidences) is subtracted, which increases the total error at the end. Furthermore, the count rate for hydrogen events is very low, so the statistical error is also quite high.

We performed a so-called slab analysis of the TOF-ERDA spectra using the software Potku². This analysis is very fast and useful when it is necessary to calculate an average concentration of elements in a homogeneous sample³. For the slab analysis, the events belonging to a particular mass in the TOF/E coincidence spectra are selected (regions of interest are created) and saved as a separate file. Each of these files contains TOF spectra for each element (the TOF axis is used for depth profiling due to better intrinsic time/energy resolution), which are then converted to energy spectra. The basis for converting energy spectra into depth profiles by slab analysis in Potku is as follows: (i) The energy axis of the energy spectra is converted to depth using the known energy stopping power data (dE/dx values). (ii) The height of the dedicated mass energy spectra (number of events per channel/energy/depth) is proportional to the element concentration multiplied by the cross-section of the interaction, the incident ion beam fluence and the solid angle of the detector. (iii) The sample is divided into a number of slabs (layers) of defined thickness. The composition of the first layer is derived from the part of all mass energy spectra corresponding to the defined slab thickness and scaled. (iv) After the first layer, the composition of the second layer is calculated, taking into account the stopping of the ions by the first layer. (v) The composition of the third and subsequent layers is calculated according to the previous procedure. The formulae involved in the calculations are beyond the scope of this paper and can be found in the study by DOYLE et al.⁴. All contributions to the depth profile, such as energy resolution of the detector, energy straggling, and multiple scattering, are not taken into account and are not deconvoluted from the depth profile. For this reason, we do not have a sharp (box) depth profile at the surface, but a depth profile convolved with all sources of energy broadening. The surface of the sample is actually at half the height of the maximum (see Fig. S1). Negative values also relate to the energy broadening of the surface edge. The stoichiometry was additionally checked using the Monte Carlo (MC) simulation software Corteo⁵. In MC, energy straggling and multiple scattering, which are not calculated by the Potku software in the slab analysis, can be simulated. Using the same SRIM-2013 stopping power data as in the slab analysis, the simulation of MC gave the same elemental composition (within the total error). Tab. S1 summarises the stoichiometries of the measured LiMO_3 crystals.

* Corresponding author.

^a Institute of Experimental Physics, TU Bergakademie Freiberg, Leipziger Str. 23, 09599 Freiberg, Germany. E-mail: thomas.koehler@physik.tu-freiberg.de

^b Institute of Applied Physics and Measurement Technology, Universität der Bundeswehr München, 85579 Neubiberg, Germany.

^c Institute of Analytical Chemistry, TU Bergakademie Freiberg, Leipziger Str. 29, 09599 Freiberg, Germany.

^d Institute of Solid State and Materials Physics, TU Dresden, Zellescher Weg 16, 01069 Dresden, Germany.

^e Application Laboratory, Eltra GmbH, Retsch-Allee 1-5, 42781 Haan, Germany.

^f Division of Experimental Physics, Laboratory for Ion Beam Interactions, Ruđer Bošković Institute, Bijenička cesta 54, 10000 Zagreb, Croatia.

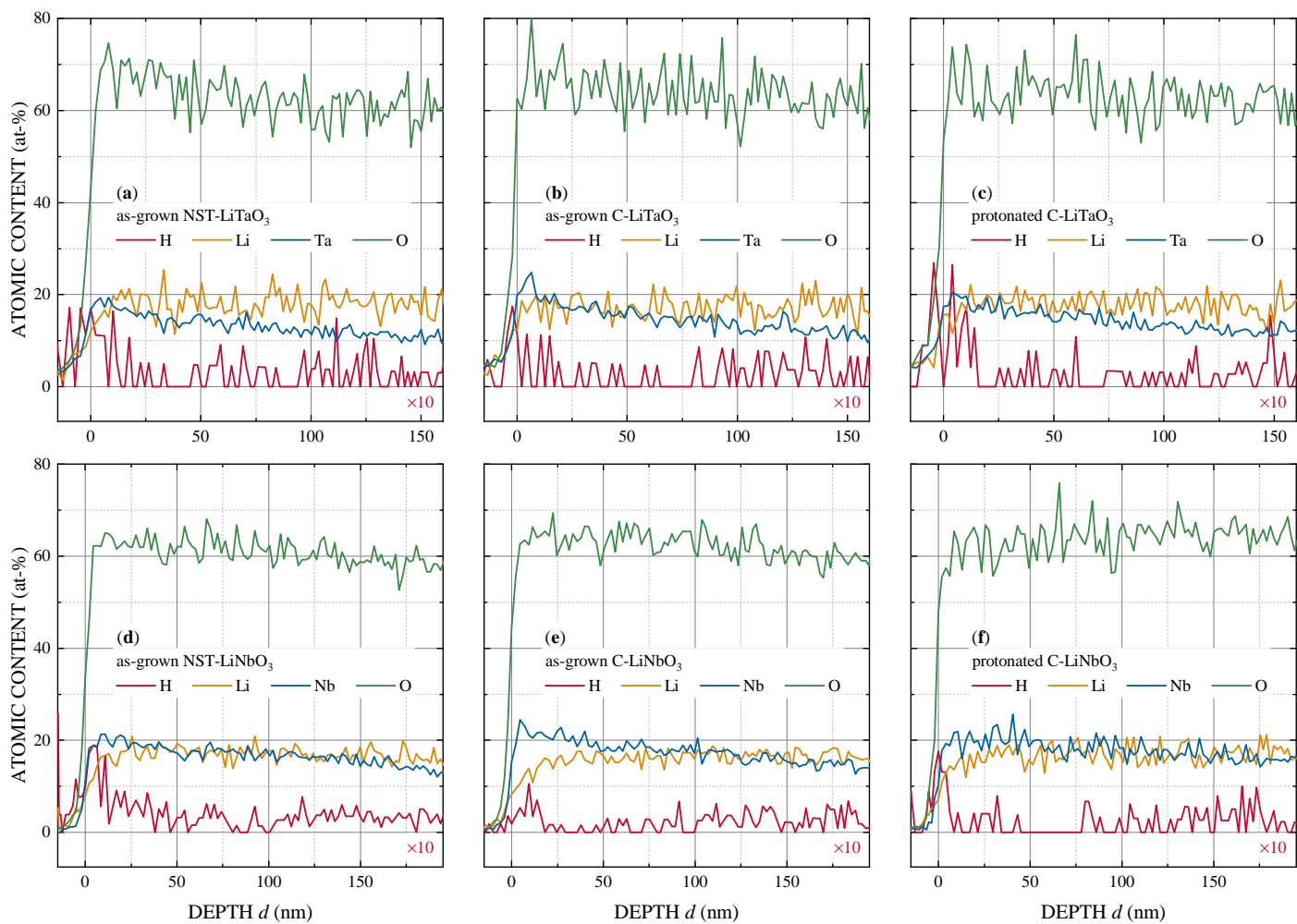


Fig. S1 Stoichiometry of (a, d) as-grown NST-LiMO₃, (b, e) as-grown C-LiMO₃ and (c, f) protonated C-LiMO₃ crystals. The atomic content over the penetration depth is equal for as-grown and protonated single crystals. For clarity, the hydrogen contents were multiplied by a factor of 10.

Table S1 Summary of the atomic content in C- and NST-LiMO₃ by TOF-ERDA.

Sample	Li (at-%)	M (at-%)	O (at-%)
as-grown C-LiNbO ₃	15.0 ± 1.6	20.3 ± 1.6	62.6 ± 4.3
protonated C-LiNbO ₃	16.1 ± 1.5	19.7 ± 2.1	61.1 ± 4.2
as-grown C-LiTaO ₃	17.0 ± 1.7	18.0 ± 1.7	65.9 ± 4.6
protonated C-LiTaO ₃	17.9 ± 1.7	17.1 ± 1.4	64.1 ± 4.5
as-grown NST-LiNbO ₃	16.7 ± 1.7	18.3 ± 1.4	61.3 ± 4.7
as-grown NST-LiTaO ₃	17.9 ± 2.1	15.7 ± 1.8	65.7 ± 5.2

S2 Error estimation for CGHE of LiMO_3 crystals

To determine the statistical uncertainty of the hydrogen content for CGHE, several crystals were measured one after the other. Fig. S2 shows the concentration for two series of C- LiMO_3 crystals of the same crystal batch. The OH^- absorption band areas determined by FT-IR are all nearly the same and amount to $(29.3 \pm 0.3) \text{ cm}^{-2}$ and $(54.8 \pm 0.6) \text{ cm}^{-2}$ for C- LiTaO_3 and C- LiNbO_3 , respectively. Based on the absorption bands, it is expected that the H concentration within the sample series should be constant. However, we find that with increasing number of samples the detected H contents increase (see Fig. S2). A spreading of volatile components was suspected and a contamination of the system has been found. This phenomenon is absolutely undesirable for element analysis using CGHE, since it makes multiple measurements impossible. We suspect that Li_2O evaporates as a volatile component when the crystals were melted. This is also known, for example, in the C- LiMO_3 crystal growth process. Li evaporates from the melt, which causes Li repulsion from the growth surface and results in the typical congruent composition of the crystal⁶. In addition, previous studies on defect incorporation have shown that desorption of Li_2O from the crystal surface is favoured during chemical reduction of C- LiMO_3 ⁷⁻¹⁰. The Li_2O appears to deposit in the measurement setup and also incorporates H species.

A valid determination of the statistical uncertainty based on a multiple measurement is not possible (see Fig. S2) and it can be assumed that this problem may be observed in the same fashion with other lithium metal oxides/compounds. In contrast to the multiple measurement of several samples in Fig. S2, we have attempted to determine an uncertainty for C- LiTaO_3 crystals by cleaning and recalibrating the system between two independent measurements, and we still obtain $\sim 33\%$ deviation for the H concentration.

For the determination of a bulk OH^- concentration, the CGHE fails due to various problems with the sample base. Despite a weaker OH^- absorption band, a significantly higher concentration is measured in C- LiTaO_3 than in C- LiNbO_3 , which cannot be considered reasonable. In contrast to the first measured concentration value (with the lowest influence by Li evaporation) of C- LiTaO_3 , the value for C- LiNbO_3 is close to the total H content of the p-p scattering method (averaged over the entire sample thickness d) only differing by a factor of ~ 2 (see Tab. 2). It can be assumed that the deviation of C- LiTaO_3 crystals is so large due to the higher melting point of the material, so that more Li evaporates before the total crystal is melted.

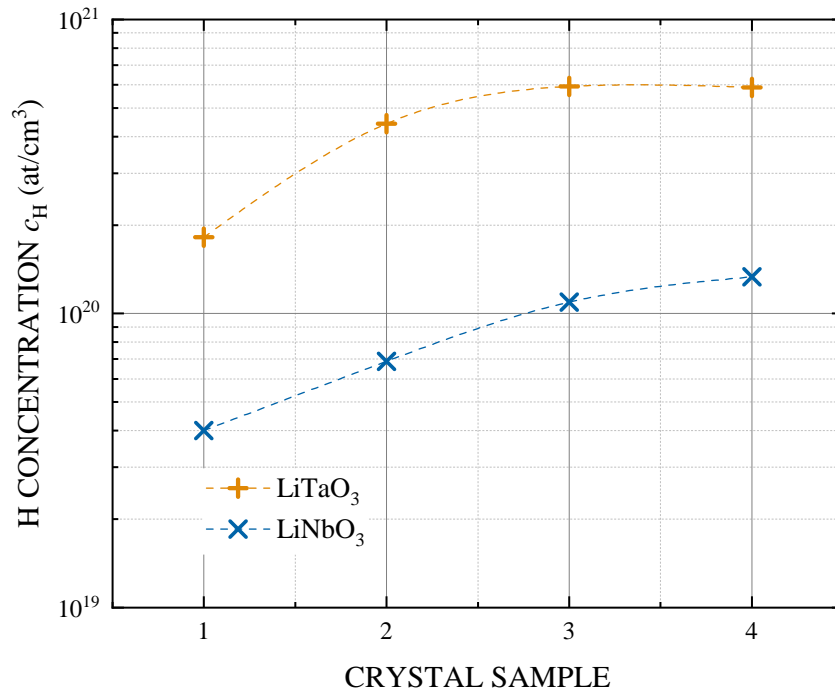


Fig. S2 Multiple CGHE measurements of two sample series of C- LiTaO_3 and C- LiNbO_3 . Between the series of measurements for C- LiTaO_3 and C- LiNbO_3 crystals, the measurement setup was cleaned and a new calibration was made.

S3 Analysis of ^1H MAS NMR spectra

The ^1H MAS signals of differently prepared powder samples made from congruent LiTaO_3 single crystals were measured. For our concentration analysis, the two references of ammonium dihydrogen phosphate ($\text{NH}_4\text{H}_2\text{PO}_4$) and disodium phosphate (Na_2HPO_4) were applied and their spectra are given in Fig. S3. For $\text{NH}_4\text{H}_2\text{PO}_4$ two types of hydrogen bonds exist: the ammonium protons and the hydrogen phosphate protons. The ^1H MAS signal consists of two lines at 7.03 ppm and 15.26 ppm, where the stronger signal can be assigned to the four protons of the ammonium group and the less shielded signal is typical for the two acidic protons in hydrogen phosphate¹¹.

The ^1H MAS signal of Na_2HPO_4 shows one line at 14.17 ppm for the hydrogen phosphate protons. The very small peak at 6.96 ppm can be assigned to a low amount of water impurities in the reference material and is not included in the integrated area of the reference.

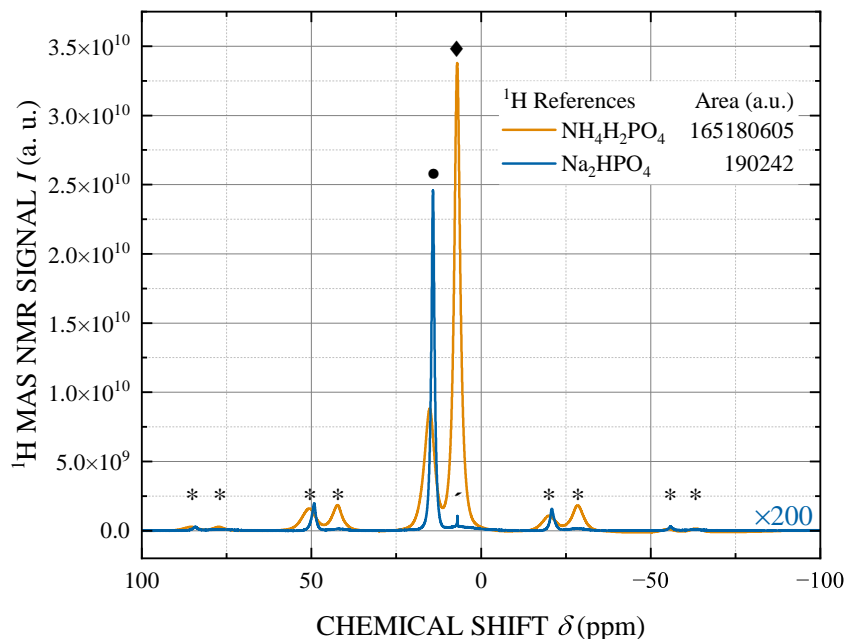


Fig. S3 ^1H MAS NMR Spectrum of $\text{NH}_4\text{H}_2\text{PO}_4$ and Na_2HPO_4 measured with a spinning speed of 14 kHz at room temperature. The symbols in the spectrum mark: \blacklozenge – ammonium protons, \bullet – hydrogen phosphate protons, \times – water, $*$ – spinning sidebands. For comparability, the spectra were scaled to the amount of substance (mol) and for optical clarity the Na_2HPO_4 data were multiplied by a factor of 200.

The preparation of the C- LiTaO_3 samples has a large influence on the resulting spectra. In general, the spectra are asymmetric and very broad, from which it can be assumed that different H containing species exist. In general, these environments can be characterised by their individual chemical shifts. Besides the structural OH^- , mobile proton groups of water can be expected. The ^1H chemical shift for a defined structure of the OH^- group is in principle unique, but in practice it should be considered that dynamic exchange effects, such as molecular rotations of the hydroxyl groups, rotation of the water or surface groups and proton transfer, cause an exchange between these different chemical shifts – this effect leads to an averaging of the line positions^{12,13}. Furthermore, the chemical shift depends strongly on the formed hydrogen bonds and on the acidity in the H containing structures¹⁴.

A fit model with one or two pseudo-VOIGT functions is applied to deconvolute the spectra (see Fig. 5). The fit values are given in Tab. S2. It can be seen that in the as-grown samples, which were milled in ambient air, two components can be found, which are assigned to mobile protons from adsorbed water and H groups of the single crystal. All samples milled under ambient air show a narrow and intense central line around 5 ppm, which is attributed to the H_2O groups due to their faster dynamic exchange processes. The adsorption of water on the powder was confirmed by DRIFTS measurements (see Sec. S4).

In contrast to the samples prepared under ambient air, the powders prepared in the Ar glovebox show only one ^1H signal. This has a lower intensity, because the H groups of the single crystal are less mobile than the adsorbed surface H_2O . It is obvious that the powder preparation under Ar significantly suppresses the contribution of adsorbed H_2O , which simplifies the evaluation of the NMR spectra with respect to the hydrogen species of the single crystal. Furthermore, the protonated samples show a broader signal than the as-grown crystals, which can be attributed to the increase in H concentration and the associated increase in homonuclear/heteronuclear dipolar interactions between the protons and ions of the host lattice.

The comparison between the determined H concentrations by NMR and p-p scattering shows that the H content from NMR is more than an order of magnitude higher. This can be explained by the fact that the used powder represents mostly a saturated surface. The results of the p-p scattering on single crystals have shown that the surfaces are strongly contaminated with H species, through

the saturation of dangling bonds with H, but also through the incorporation of impurities/defects by polishing of the crystals. These impurities are also retained in the single crystal signal of the prepared powders under ambient air and Ar atmosphere. Thus, in a first approximation, the concentration at the surfaces from the p-p scattering can be directly compared with the NMR signal. In our p-p scattering results we obtain an averaged H concentration of $\sim (6 \pm 2) \cdot 10^{19}$ at/cm³ in the first 5 μ m of the single crystal surfaces. It can be assumed that due to the increased surface-to-volume ratio of the powders, the ¹H NMR spectra of the samples from ambient air are significantly dominated by the surface H species. Samples prepared in the Ar atmosphere show a reduction in their H₂O content, but this seems not to be completely suppressed and, together with the H species present on the single crystal surfaces (see Sec. S4), influences the quantitative analysis. An exact determination of the OH⁻ bulk concentration could be achieved e. g. by ¹H MAS measurements on a cylindrical single crystal, which is directly cut in shape for a ZrO₂ MAS rotor.

Table S2 Analysis of ¹H MAS NMR signals of as-grown and protonated LiTaO₃ powder. Here, δ is the peak position, A is the peak area, Γ is the FWHM and the G/L ratio describes the mixture of both profile functions (the value is 1 for GAUSSIAN and 0 for LORENTZIAN). The peak area A is given for the isotropic central line (CL) and also in total including the spinning sidebands (SSB). The assignment of the deconvolution to adsorbed water on the surface and the H species of the single crystal are labelled H₂O and SC, respectively. The calculated hydrogen concentration c_H is given with respect to the H species of the single crystal.

Sample	δ (ppm)	A_{CL} (a. u.)	A_{CL+SSB} (a. u.)	Γ (ppm)	G/L ratio	c_H (10^{19} at/cm ³)
as-grown – mortar	H ₂ O: 4.90 ± 0.1	91861 ± 1170	93393 ± 1386	1.64 ± 0.01	0.88 ± 0.02	8.0 ± 1.0
	SC: 5.14 ± 0.1	190247 ± 4647	215627 ± 5634	7.26 ± 0.14	0.61 ± 0.01	
as-grown – ball mill	H ₂ O: 4.79 ± 0.1	88221 ± 4491	90374 ± 4910	2.24 ± 0.06	0.43 ± 0.06	9.1 ± 1.2
	SC: 5.45 ± 0.1	205759 ± 6466	248548 ± 7947	7.43 ± 0.14	0.52 ± 0.02	
as-grown – Ar atmosphere	SC: 4.88 ± 0.1	192938 ± 1168	227907 ± 1682	7.55 ± 0.02	0.64 ± 0.01	8.4 ± 0.9
H-doped – mortar	H ₂ O: 5.08 ± 0.1	231668 ± 1613	233651 ± 1976	2.14 ± 0.01	0.52 ± 0.01	17.1 ± 2.0
	SC: 5.28 ± 0.1	415475 ± 4243	466379 ± 5185	9.70 ± 0.05	0.76 ± 0.01	
H-doped – Ar atmosphere	SC: 4.42 ± 0.1	344953 ± 1349	372799 ± 1893	9.34 ± 0.01	0.53 ± 0.01	13.7 ± 1.5

S4 Diffuse reflectance infrared Fourier transform spectroscopy (DRIFTS) of C-LiTaO₃ powder

The NMR measurements of the C-LiTaO₃ powder have shown that the powder preparation has a strong influence on the spectra. We assume that the signal of the bulk OH⁻ defect is superimposed by adsorbed water. This assumption was additionally investigated by diffuse reflectance infrared fourier transform spectroscopy (DRIFTS). For this purpose, the powder is directly measured in a diffuse reflection unit. Fig. S4 shows the spectrum of the C-LiTaO₃ powder from the ball mill and for comparison the diffuse reflection from a C-LiTaO₃ single crystal plate. Both spectra are measured on a Bruker Tensor 27 in a range of 4000 ... 380 cm⁻¹ with a resolution of 2 cm⁻¹. It can be clearly seen that the structural OH⁻ band is overlaid by a very broad water signal for the powder. Additionally, a small contribution of C-H vibrations can be detected, which is already present on the single crystal surfaces (directly measured from the packaging of the manufacturer), but plays only a minor role compared to the adsorbed H₂O. Therefore, it is necessary for quantitative NMR to fit the peaks with at least two components. It can be seen from the DRIFTS measurements that the structural bulk OH⁻ defect contributes only ~1% to the total area of the powder spectrum. If we consider the total integrals of the NMR spectra of the as-grown powder from ambient air (see Fig. 5 a and b), a total H concentration of ~1.25 · 10²⁰ at/cm³ is determined and for a contribution of ~1% to this spectrum, the concentration would be ~1.25 · 10¹⁸ at/cm³, which is comparable to the result of the p-p scattering experiments (see Tab. 2). This estimation confirms that the powders from ambient air are predominantly H₂O saturated surfaces. To reduce the H₂O content, powders were also prepared in a glovebox under argon atmosphere. It was observed that the ¹H MAS signal decreases by ~31 ... 48% (see Sec. 5), which can be attributed to the reduction of adsorbed water. Considering these results in relation to the DRIFTS measurement, it seems that the bulk OH⁻ defect is overlaid by more hydrogen containing species than just 31%. Obviously, other H species besides the structural bulk OH⁻ remain in the powder, which dominate the spectrum and limit the comparability with the p-p scattering data. Due to the poor spectral resolution of the ¹H MAS signal, a further separation of the bulk OH⁻ is not possible.

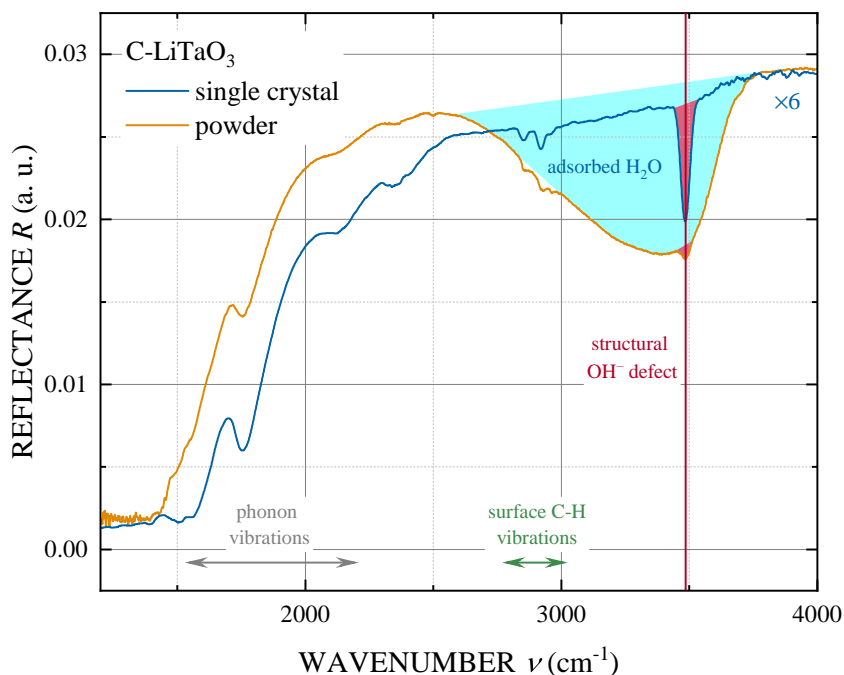


Fig. S4 IR diffuse reflection spectra of C-LiTaO₃ single crystal and powder from the ball mill. The areas of adsorbed surface water and the structural bulk OH⁻ defect were highlighted in blue and red, respectively. For clarity, the DRIFTS spectrum of the single crystal was scaled by a factor of 6 in intensity.

S5 Data analysis for p-p scattering experiments

Fig. S5 shows all measured spectra of the used LiMO_3 single crystals as well as the areas of the evaluated ROI and the background areas in the low and high energy range. The ROI were selected in a range of 15 ... 25 μm depending on the sample thickness. The ranges were chosen so that the edges of the two surface peaks do not mix into the evaluation of the bulk OH^- . The data of the surface peak of the front side (left side in the low energy range) shows a higher broadening than the peak of the back side of the sample (right side in the high energy range). The broadening is associated with multiple scattering with energy loss through the sample volume and the corresponding increase in energy blurring. To avoid this energy loss scattering in the evaluation – the right shoulder of the left surface peak – the ROI was slightly shifted to higher energies. It can be seen from all surface peaks that the hydrogen concentration at the surfaces varies up to a factor of four. The variations are mainly caused by the surface roughness (see NST- LiMO_3 in Fig. S5). The samples were ground to a thickness between 35 ... 52 μm for the p-p scattering experiments, where this side has an increased roughness, while the opposite side is polished. Surface concentrations can vary due to the degree of roughness, treatment/temperature during the polishing procedure or different conditions during storage, handling and measurement, like temperature and atmosphere¹⁵⁻¹⁹. This is why an accurate surface concentration cannot be measured reliably, unless a uniform procedure for surface cleaning is used.

For the NST crystals, the spectra for the flipped samples are also shown, whereby side 1 of the NST- LiTaO_3 is already shown in Fig. 7b. It can be seen from the flipped samples that there is a homogeneous bulk H concentration. However, since the scanned area does not match after flipping, the surface hydrogen contamination varies locally.

Uncertainty evaluation: Uncertainties in the quantification arise from two different sources. The correction function described in the main document (see Sec. 6.2) depends on the incident proton energy in combination with the density, composition and thickness of the sample. The application of the correction function from zoisite as a well characterized hydrogen-rich reference mineral to the measured sample is possible within a systematical uncertainty of about 20 %, also including the uncertainty of the beam dose and a possible deviation from the nominal stoichiometric H content of the used zoisite. This has been validated by cross referencing studies and Monte-Carlo simulations²⁰. A statistical uncertainty has to be taken into account due to counting statistics of the coincidence events. Using GAUSSIAN approximation this is the square root of the number of events. For low numbers (~ 10 events), POISSON statistics has to be applied. But in these cases, the background of accidental coincidences is in the same range as the signal and an upper limit is given from GAUSSIAN approximation (uncertainty of background signal included). Both, systematical and statistical uncertainties have a GAUSSIAN distribution and are quadratically summed up as independent GAUSSIAN uncertainties.

Evaluation of background due to accidental coincidences: The evaluation of the background in the region of interest is difficult due to the inhomogenous distribution of accidental coincidences in the overall energy sum range (Fig. 7 a). At low values for the proton energy sum (< 18 MeV for 20 MeV incident protons or $d < 0$ in depth-calibrated spectra) there appears an increased number of accidental coincidences due to protons or other particles emerging from nuclear reactions. As these accidental coincidences from nuclear reactions do not overlap with true elastic p-p events with energy sum > 18 MeV, this background level is not a measure for the background of the hydrogen content at $d > 0$ μm (see Fig. S5, especially the deprotonated crystals in d and g). For evaluation of the background for $d > 0$ μm we compare to events with “impossible” sum energy larger than the maximum incident energy of > 20 MeV. These energy sums arise from accidental coincidences from elastic scattering events and surely not from true hydrogen events. Corresponding depth values for this “impossible” proton energy sum are larger than approximately 60 μm . For the approximation of the number of background events a region is evaluated that is similar to the thickness of the region of interest in the bulk area of the sample. Note, that this region is chosen as close as possible to the high energy surface peak, as the accidental coincidences disappear completely at higher energy sums and would lower the average background in an artificial way.

The evaluated background level is subtracted from the hydrogen counts in the region of interest (statistical errors of the counts and background are considered for uncertainty evaluation). However, as the background is also affected from the correction function described in Sec. 6.2, the background in the ROI is artificially increased with this correction function compared to the background evaluation at “impossible” energy sums. This increase is considered for the background subtraction at the depth of the ROI.

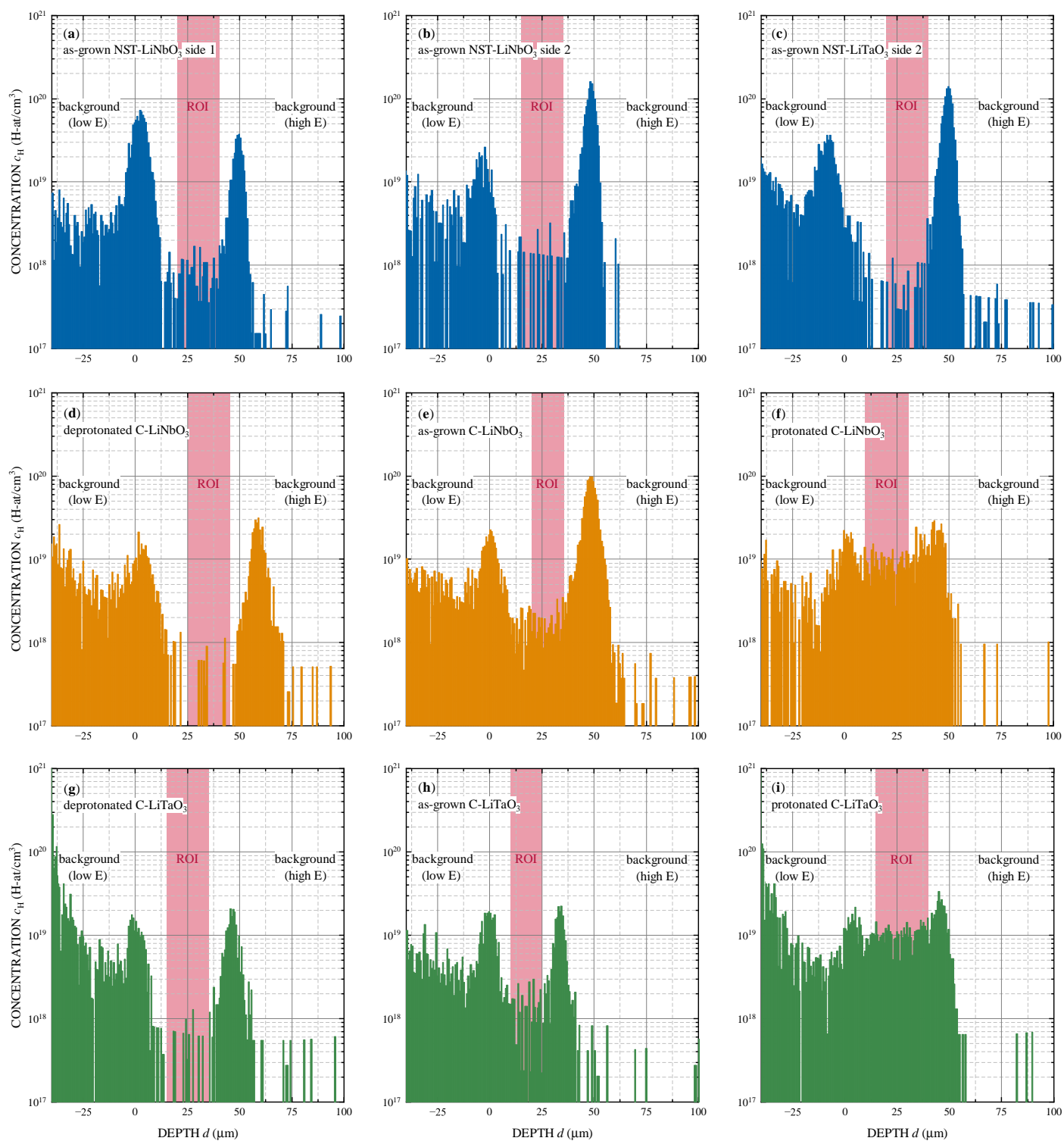


Fig. S5 The projection of the scattering events into the hydrogen depth profile of the NST- and C-LiMO₃ single crystals. The area for the analysis of the inner crystal region (ROI) are marked.

S6 Spectral analysis of FT-IR absorption bands

In this work, the OH^- absorption bands of different LiMO_3 crystals were investigated with respect to their stoichiometry and hydrogen contents. The protonation of the materials is carried out in a furnace with a wet atmosphere at 900°C for 10 h. The hydrogen concentration is significantly increased by this treatment (see Tab. S3). The shape of the OH^- absorption bands of the LiMO_3 crystals strongly depends on the $[\text{Li}]/[\text{M}]$ ratio of the materials. It is well known that the stretching vibrational modes are very narrow for the near-stoichiometric materials, while the congruent crystals show a very broad absorption band^{21–24}. This broadening mechanism was attributed to the defect clusters due to the deficiency of lithium and the decoration of the defect sites by hydrogen^{25,26}. Due to the dependence of the spectral shape on the stoichiometry, we use the area under the OH^- absorption band for the determination of the FT-IR calibration value and not the OH^- peak maximum, which was used in previous literature^{27–33}. For the FT-IR measurements we use a KRS-5 polariser, because the OH^- absorption band shows an anisotropic nature.

Tab. S3 summarises all used crystals with respect to the analytical method in which their H content was investigated. Very comparable absorption band areas are observed for the as-grown C- LiMO_3 crystals. It is obvious that the as-grown NST samples have a significantly lower absorption band than their congruent counterparts. This is not surprising, since a lower defect density is to be expected in these, i. e. there are less sites available for hydrogen decoration. The absorption band of the near-stoichiometric material is approx. 60 % and 94 % lower than in the congruent LiNbO_3 and LiTaO_3 , respectively. The fact that the lowest OH^- absorption band is measured for the as-grown NST- LiTaO_3 can be explained by the fact that this material has the highest Li content of all used crystals and thus should have the lowest concentration of intrinsic defects. The OH^- absorption mode in NST- LiTaO_3 is mainly determined by the decoration of extrinsic defects²⁶.

Table S3 Summary of the integral areas of the OH^- absorption band for C- and NST- LiMO_3 crystals and their use for different hydrogen-sensitive methods. The errors are given in 1σ standard deviation.

Method	Sample	A (cm^{-2})
p-p scattering	NST- LiNbO_3	29.2 ± 0.7
	C- LiNbO_3	77.2 ± 1.7
	prot. C- LiNbO_3	450.2 ± 10.1
	NST- LiTaO_3	4.7 ± 0.1
	C- LiTaO_3	74.4 ± 1.7
	prot. C- LiTaO_3	758.6 ± 17.1
NMR	C- LiTaO_3	88.3 ± 2.0
	prot. C- LiTaO_3	453.3 ± 10.2
CGHE	C- LiNbO_3	54.9 ± 1.2
	C- LiTaO_3	79.4 ± 1.7
	prot. C- LiTaO_3	505.7 ± 11.4
ERDA	NST- LiNbO_3	30.4 ± 0.7
	C- LiNbO_3	70.8 ± 1.6
	prot. C- LiNbO_3	289.7 ± 6.5
	NST- LiTaO_3	4.2 ± 0.1
	C- LiTaO_3	156.1 ± 3.5
	prot. C- LiTaO_3	474 ± 10.7

Notes and references

- 1 J. F. Ziegler, Nuclear Instruments and Methods in Physics Research Section B: Beam Interactions with Materials and Atoms, 2004, **219–220**, 1027 – 1036.
- 2 K. Arstila, J. Julin, M. Laitinen, J. Aalto, T. Konu, S. Kärkkäinen, S. Rahkonen, M. Raunio, J. Itkonen, J.-P. Santanen, T. Tuovinen and T. Sajavaara, Nuclear Instruments and Methods in Physics Research Section B: Beam Interactions with Materials and Atoms, 2014, **331**, 34–41.
- 3 Y. Wang and M. Nastasi, Handbook of Modern Ion Beam Materials Analysis, Materials Research Society, 2010.
- 4 B. Doyle and D. Brice, Nuclear Instruments and Methods in Physics Research Section B: Beam Interactions with Materials and Atoms, 1988, **35**, 301 – 308.
- 5 F. Schiettekatte, Nuclear Instruments and Methods in Physics Research Section B: Beam Interactions with Materials and Atoms, 2008, **266**, 1880 – 1885.
- 6 P. Bordui, R. Norwood, C. Bird and J. Carella, Journal of Applied Physics, 1995, **78**, 4647–4650.
- 7 K. Tabata, T. Choso and Y. Nagasawa, Surface Science, 1998, **408**, 137–145.
- 8 Y. Yun, M. Li, D. Liao, L. Kampschulte and E. Altman, Surface Science, 2007, **601**, 4636–4647.
- 9 L. Kocsor, L. Péter, G. Corradi, Z. Kis, J. Gubicza and L. Kovács, Crystals, 2019, **9**, 334.
- 10 T. Köhler, M. Zschornak, M. Zbiri, J. Hanzig, C. Röder, C. Funke, H. Stöcker, E. Mehner and D. C. Meyer, Journal of Materials Chemistry C, 2021, **9**, 13484–13499.
- 11 A. R. Lim and K.-S. Lee, Solid State Sciences, 2013, **21**, 54–58.
- 12 B. Grünberg, T. Emmeler, E. Gedat, I. Shenderovich, G. H. Findenegg, H.-H. Limbach and G. Buntkowsky, Chemistry – A European Journal, 2004, **10**, 5689–5696.
- 13 A. Vyalikh, T. Emmeler, B. Grünberg, Y. Xu, I. Shenderovich, G. Findenegg, H.-H. Limbach and G. Buntkowsky, Zeitschrift für Physikalische Chemie, 2007, **221**, 155–168.
- 14 P. Batamack, C. Doremieux-Morin, R. Vincent and J. Fraissard, The Journal of Physical Chemistry, 1993, **97**, 9779–9783.
- 15 G. Dollinger, M. Boulouednine, A. Bergmaier, T. Faestermann and C. Frey, Nuclear Instruments and Methods in Physics Research Section B: Beam Interactions with Materials and Atoms, 1996, **118**, 291–300.
- 16 G. Dollinger, C. Frey, A. Bergmaier and T. Faestermann, Europhysics Letters, 1998, **42**, 25.
- 17 R. Behrisch, M. Mayer, W. Jacob, W. Assmann, G. Dollinger, A. Bergmaier, U. Kreissig, M. Friedrich, G. Sun, D. Hildebrandt, M. Akbi, W. Schneider, D. Schleußner, W. Knapp and C. Edelmann, Journal of Nuclear Materials, 2000, **281**, 42–56.
- 18 A. Bergmaier, G. Dollinger, A. Aleksov, P. Gluche and E. Kohn, Surface Science, 2001, **481**, L433–L436.
- 19 P. Reichart, G. Dollinger, G. Datzmann, A. Hauptner, R. Hertenberger and H.-J. Körner, Nuclear Instruments and Methods in Physics Research Section B: Beam Interactions with Materials and Atoms, 2003, **210**, 135–141.
- 20 M. Moser, P. Reichart, A. Bergmaier, C. Greubel, F. Schiettekatte and G. Dollinger, Nuclear Instruments and Methods in Physics Research Section B: Beam Interactions with Materials and Atoms, 2016, **371**, 161–166.
- 21 L. Kovács, M. Wöhlecke, A. Jovanović, K. Polgár and S. Kapphan, Journal of Physics and Chemistry of Solids, 1991, **52**, 797 – 803.
- 22 C. Bäumer, C. David, K. Betzler, H. Hesse, K. Lengyel, L. Kovács and M. Wöhlecke, physica status solidi (a), 2004, **201**, R13–R16.
- 23 L. Shi, W. Yan and Y. Kong, European Physical Journal – Applied Physics, 2007, **40**, 77–82.
- 24 T. Köhler, E. Mehner, J. Hanzig, G. Gärtner, C. Funke, Y. Joseph, T. Leisegang, H. Stöcker and D. C. Meyer, Journal of Materials Chemistry C, 2021, **9**, 2350–2367.
- 25 T. Köhler, E. Mehner, J. Hanzig, G. Gärtner, H. Stöcker, T. Leisegang and D. Meyer, Journal of Solid State Chemistry, 2016, **244**, 108 – 115.
- 26 T. Köhler, M. Zschornak, C. Röder, J. Hanzig, G. Gärtner, T. Leisegang, E. Mehner, H. Stöcker and D. C. Meyer, Journal of Materials Chemistry C, 2023, **11**, 520–538.
- 27 W. Bollmann, K. Schlothauer and O. J. Zogal, Kristall und Technik, 1976, **11**, 1327–1332.
- 28 L. Kovács, Z. Szaller, I. Cravero, I. Földvári and C. Zaldo, Journal of Physics and Chemistry of Solids, 1990, **51**, 417 – 420.
- 29 G. Mandula, M. A. Ellabban and M. Fally, Ferroelectrics, 2007, **352**, 118–124.
- 30 R. Müller, L. Arizmendi, M. Carrascosa and J. M. Cabrera, Applied Physics Letters, 1992, **60**, 3212–3214.
- 31 R. Richter, T. Bremer, P. Hertel and E. Krätzig, physica status solidi (a), 1989, **114**, 765–774.
- 32 S. Klauer, M. Wöhlecke and S. Kapphan, Physical Review B, 1992, **45**, 2786–2799.
- 33 S. Kapphan and A. Breitenkopf, physica status solidi (a), 1992, **133**, 159–166.